SAND2005-7942C

Large Eddy Simulation of Swirling Particle-Laden Flow in a Model Axisymmetric Combustor

Joseph C. Oefelein

Combustion Research Facility
Sandia National Laboratories, Livermore, CA 94551-9051 USA

Corresponding Author:

Joseph C. Oefelein
Combustion Research Facility
Sandia National Laboratories
P.O. Box 969, Mail Stop 9051
Livermore, CA 94551-9051 USA
Tel: (925) 294-2648
Fax: (925) 294-2595
Email: *oefelei@sandia.gov*

Paper ID Number: PID153716

Name of Colloquium: Spray and Droplet Combustion

Short Running Title: LES of Sprays in Confined Swirling Flows

Total Length of Paper: 5684 words (obtained using method 2, LaTeX two-column procedure).
Main text, equations and acknowledgements: 4100
Nomenclature: 0
References: 275
Figures: $286 + 88 + 110 + 286 + 88 + 66 + 66 + 66 + 66 + 66 + 66 + 220 = 1474$
Tables: 110

Keywords: LES; Spray modeling; Swirling particle-laden flow

Submitted for presentation at the
31st International Symposium on Combustion
University of Heidelberg, Germany, August 6-11, 2006

Abstract

Modeling multiphase combustion processes using the Large Eddy Simulation *(LES)* technique poses a variety of challenges due to the complex nonlinear nature of the phenomena involved. Multiple strongly coupled processes exist in close proximity to one another and interact over wide ranges of time and length scales. The situation is compounded by the presence of dynamically evolving interface boundaries and the intricate exchange processes that occur as a consequence. As part of an effort to treat these phenomena systematically, a series of LES calculations have been performed and compared directly with experimental data. These experiments characterize a swirling particle-laden flow in a model coaxial combustion chamber and effectively isolate effects related to dilute particle dispersion and momentum coupling. The validated case study and methodologies presented provide a clearer understanding of the effectiveness and feasibility of current state-of-the-art models and a quantitative understanding of relevant modeling issues by analyzing the characteristic parameters and scales of importance. The novel feature of the results presented is that they establish a baseline level of confidence in our ability to simulate complex flows at conditions representative of those typically observed in gas-turbine (and similar) combustors.

1. Introduction

Obtaining high-fidelity solutions of reacting sprays hinges on the application of methods and models that accurately describe momentum coupling and subgrid-scale *(sgs)* modulation of turbulence, mass and energy coupling and *sgs* scalar mixing, and the turbulent combustion processes induced as a consequence. As part of an effort to treat these phenomena systematically, the current work focuses on a swirling particle-laden flow in a model coaxial combustion chamber. A series of Large Eddy Simulation *(LES)* calculations have been performed and compared to the experimental data acquired by Sommerfeld *et al*. [1–3]. The primary objectives are to gain a clearer understanding of the effectiveness and feasibility of current state-of-the-art *sgs* models and a quantitative understanding of potential model limitations and future needs when applied in a complex flow configuration.

Sommerfeld *et al*. provide detailed measurements of swirling particle-laden flow in a model combustion chamber that consists of a sudden pipe expansion with a centered (primary) and annular (secondary) jet discharging into a cylindrical test section. The experimental measurements were acquired using a one-component phase-Doppler-anemometer *(PDA)* to obtain mean and rms gas-phase and particle-phase statistics of velocity and particle size. These data provide two excellent benchmark cases for validation of LES in a turbulent swirling-flow environment very similar to the flow in a gas turbine combustor, under highly controlled conditions, and with well-defined boundary conditions. They provide a way to systematically validate LES models for unsteady dilute spray dynamics without having to simultaneously treat the more complex issues related to atomization, secondary breakup, and coupling between the gas and particulate phases under highly loaded conditions. Establishing this level of validation is a key progressive step toward treating these more daunting issues.

Past numerical studies have focused on particle-turbulence interactions in simplified geometries [4–6], with emphasis placed on the effects of gas-phase velocity fluctuations on particle dispersion characteristics, the preferential concentration of particles, and the influence of particles on the turbulence energy spectra. We have also performed a series of studies [7–10] focused on the development of high-performance massively parallel numerical algorithms to support the implementation of high-fidelity LES calculations. Considerable experimental work on turbulent particle-laden flows has also been performed [11].

More recently [12], we have systematically evaluated and improved our treatment of dilute spray dynamics under highly loaded conditions through careful comparison to the data acquired in the fully-developed channel flow experiments of Paris and Eaton [13] and Benson and Eaton [14]. Here, we extend these analyses by applying the most recent modeling approach in a validated state-of-the-art theoretical-numerical framework that has been optimized for the application of LES for general treatment of turbulent reacting multiphase flows at practical conditions. Emphasis is placed on establishing the predictive nature of the coupled set of *sgs* models in a manner that lends itself to treatment of more complex systems and phenomena.

2. Theoretical Framework

2.1. Governing Conservation Equations

The simulations were performed using the theoretical-numerical framework developed by Oefelein [15, 16]. This framework is optimized to meet the strict algorithmic requirements imposed by the LES formalism and provide a unified treatment of turbulent reacting multiphase flows over a wide range of conditions. The general form of the governing system is assumed to be compressible, chemically reacting, and composed of N species. For the most general cases, we solve the fully-coupled conservation equations. These equations are combined with an appropriate equation of state, thermodynamic and transport properties, and validated mixing rules for the mixtures of interest.

The governing system is cast in dimensionless form using a reference length-scale $\delta_{\rm ref}$, flow speed $U_{\rm ref}$, and fluid state characterized by a reference density $\rho_{\rm ref}$, sound speed $c_{\rm ref}$, constant pressure specific heat

$C_{p_{\rm ref}}$, and dynamic viscosity $\mu_{\rm ref}$. For LES applications the instantaneous conservation equations are filtered yielding the following system of equations for mass, momentum, total-energy and species, respectively:

$$\frac{\partial}{\partial t}(\theta\overline{\rho}) + \nabla\cdot(\theta\overline{\rho}\tilde{\mathbf{u}}) = \overline{\dot{\rho}}_s, \tag{1}$$

$$\begin{aligned}\frac{\partial}{\partial t}(\theta\overline{\rho}\tilde{\mathbf{u}}) &+ \nabla\cdot\left[\theta\left(\overline{\rho}\tilde{\mathbf{u}}\otimes\tilde{\mathbf{u}} + \frac{\mathcal{P}}{M^2}\mathbf{I}\right)\right] \\ &= \nabla\cdot(\theta\vec{\vec{\mathcal{T}}}) + \overline{\dot{\mathbf{F}}}_s,\end{aligned} \tag{2}$$

$$\begin{aligned}\frac{\partial}{\partial t}(\theta\overline{\rho}\tilde{e}_t) &+ \nabla\cdot[\theta(\overline{\rho}\tilde{e}_t + \mathcal{P})\tilde{\mathbf{u}}] \\ &= \nabla\cdot\left[\theta\left(\vec{\mathcal{Q}}_e + M^2(\vec{\vec{\mathcal{T}}}\cdot\tilde{\mathbf{u}})\right)\right] \\ &+ \theta\overline{\dot{Q}}_e + \overline{\dot{Q}}_s, \text{ and}\end{aligned} \tag{3}$$

$$\begin{aligned}\frac{\partial}{\partial t}(\theta\overline{\rho}\tilde{Y}_i) &+ \nabla\cdot(\theta\overline{\rho}\tilde{Y}_i\tilde{\mathbf{u}}) \\ &= \nabla\cdot(\theta\vec{\mathcal{S}}_i) + \theta\overline{\dot{\omega}}_i + \overline{\dot{\omega}}_{s_i}.\end{aligned} \tag{4}$$

The terms θ, $\overline{\dot{\rho}}_s$, $\overline{\dot{\mathbf{F}}}_s$, $\overline{\dot{Q}}_s$ and $\overline{\dot{\omega}}_{s_i}$ represent the filtered void fraction and spray source terms that account for interphase exchange of mass, momentum, total energy and species, respectively. The terms $\mathcal{P}$,$\vec{\vec{\mathcal{T}}}$, $\vec{\mathcal{Q}}_e$ and $\vec{\mathcal{S}}_i$ are respective composite (i.e., molecular plus *sgs*) stresses and fluxes. The terms $\overline{\dot{Q}}_e$ and $\overline{\dot{\omega}}_i$ are the filtered energy and species source terms.

2.2. Subgrid-Scale Closure

The current *sgs* closure is obtained using the mixed dynamic Smagorinsky model by combining the models proposed by Erlebacher *et al*. [17] and Speziale [18] with the dynamic modeling procedure [19–23]. The composite stresses and fluxes in Eqs. (1)–(4) are given as

$$\begin{aligned}\vec{\vec{\mathcal{T}}} &= (\mu_t+\mu)\frac{1}{Re}\left[-\frac{2}{3}(\nabla\cdot\tilde{\mathbf{u}})\mathbf{I} + \left(\nabla\tilde{\mathbf{u}} + \nabla\tilde{\mathbf{u}}^T\right)\right] \\ &\quad -\overline{\rho}\left(\widetilde{\tilde{\mathbf{u}}\otimes\tilde{\mathbf{u}}} - \tilde{\tilde{\mathbf{u}}}\otimes\tilde{\tilde{\mathbf{u}}}\right),\end{aligned} \tag{5}$$

$$\begin{aligned}\vec{\mathcal{Q}}_e &= \left(\frac{\mu_t}{Pr_t} + \frac{\mu}{Pr}\right)\frac{1}{Re}\nabla\tilde{h} + \sum_{i=1}^{N}\tilde{h}_i\vec{\mathcal{S}}_i \\ &\quad -\overline{\rho}\left(\widetilde{\tilde{h}\tilde{\mathbf{u}}} - \tilde{\tilde{h}}\tilde{\tilde{\mathbf{u}}}\right), \text{ and}\end{aligned} \tag{6}$$

$$\begin{aligned}\vec{\mathcal{S}}_i &= \left(\frac{\mu_t}{Sc_{t_i}} + \frac{\mu}{Sc_i}\right)\frac{1}{Re}\nabla\tilde{Y}_i \\ &\quad -\overline{\rho}\left(\widetilde{\tilde{Y}_i\tilde{\mathbf{u}}} - \tilde{\tilde{Y}}_i\tilde{\tilde{\mathbf{u}}}\right).\end{aligned} \tag{7}$$

Here, the term μ_t is the *sgs* eddy viscosity given by the relation

$$\mu_t = \overline{\rho}C_R\Delta^2\Pi_{\tilde{\mathbf{S}}}^{\frac{1}{2}}, \tag{8}$$

where

$$\Pi_{\tilde{\mathbf{S}}} = \tilde{\mathbf{S}} : \tilde{\mathbf{S}}, \text{ and } \tilde{\mathbf{S}} = \frac{1}{2}\left(\nabla\tilde{\mathbf{u}} + \nabla\tilde{\mathbf{u}}^T\right). \tag{9}$$

The terms C_R, Pr_t, and Sc_{t_i} are the Smagorinsky, *sgs*-Prandtl and *sgs*-Schmidt numbers and are evaluated dynamically as functions of space and time. There are no tuned constants employed anywhere in the closure. The overall model includes the Leonard and cross-term stresses and provides a Favre averaged generalization of the Smagorinsky model [24].

2.3. Lagrangian Particle Model

To handle the particulate phase, Lagrangian particle models for momentum are employed using the fundamental framework developed by Oefelein [10]. The source term $\overline{\dot{\mathbf{F}}}_s$ in Eq. (2) accounts for the interphase exchange of momentum imposed by the particles on the resolved-scales. For particles on the order of, or smaller than, the Kolmogorov scale, this term is given by an expression of the form

$$\overline{\dot{\mathbf{F}}}_s(\mathbf{x},t) = \underbrace{\int_t^{t+\Delta t} \underbrace{\sum_p \mathcal{G}(\mathbf{y}_p - \mathbf{x}, \tau - t)\ \underbrace{\left\{ m_p \frac{d\mathbf{u}_p}{d\tau} \right\}}_{(i)}}_{(ii)} d\tau}_{(iii)}. \tag{10}$$

The quantity $\mathcal{G}$ is the filter function. Term (i) represents the instantaneous force induced by respective particles at remote points $\mathbf{y}_p$ and times τ. Term (ii) represents the spatially filtered effect of these remote exchange processes on discrete points $\mathbf{x}$ within the volume of influence defined by the filter. Term (iii) represents the filtered effect of *sgs* temporal disturbances over the integration time-step $\delta\tau$.

Explicit filtering of the particulate phase is performed using a top-hat filter. This is analogous to the particle-source-in-cell methodology developed by Crowe *et al.* [25]. The term $\sum_p$ in Eq. (10) represents a summation over all discrete particles within a given finite-volume cell. This approximation was found to be acceptable for the cases considered since the particle loading is relatively low. Particle dynamics are simulated assuming that 1) the density of the particles is much greater than the density of the carrier fluid, 2) the particles are dispersed and collisions between particles are negligible, 3) the particles are on the order of, or smaller than, the Kolmogorov scale in size, and 4) that particle motion due to shear is negligible. Under these assumptions the Lagrangian equations which govern instantaneous particle motion can be written as

$$\frac{d\mathbf{x}_p}{d\tau} = \mathbf{u}_p, \tag{11}$$

$$\frac{d\mathbf{u}_p}{d\tau} = \frac{\tau_f}{\tau_r}\left(\mathbf{u} - \mathbf{u}_p\right) + \mathbf{g}. \tag{12}$$

These equations are non-dimensionalized using the same reference quantities used in Eqs. (1)–(4). The subscript p denotes values associated with individual particles. The ratio τ_r/τ_f (where $\tau_f = \delta_{\text{ref}}/U_{\text{ref}}$) is the dimensionless particle relaxation time

$$\frac{\tau_r}{\tau_f} = \frac{St}{(1 + a_p Re_p^{b_p})}. \tag{13}$$

The term St is the Stokes number based on the mean flow time scale τ_f, i.e.,

$$St = \frac{\tau_p}{\tau_f} = \frac{1}{18}\rho_p d_p^2 Re. \tag{14}$$

The quantities ρ_p and d_p are the dimensionless particle density and diameter, respectively. The term Re_p is the particle Reynolds number, where

$$Re_p = d_p Re \left| \mathbf{u} - \mathbf{u}_p \right|. \tag{15}$$

The instantaneous drag acting on respective particles is modeled using the nonlinear correlation given by Schiller and Nauman [26]. Using this correlation Eq. (13) is evaluated using $a_p = 0.15$ and $b_p = 0.687$. This correlation matches the standard drag curve to within $\pm 4\%$ on the interval $Re_p < 800$.

Equations (11) and (12) are integrated using a fourth-order Runge-Kutta time-stepping technique applied in a manner consistent with the evaluation of the explicit terms in the gas-phase solver. The instantaneous velocity field is approximated by reconstructing Favre decompositions of the form $\mathbf{u} = \tilde{\mathbf{u}} + \mathbf{u}''$ using tri-linear interpolation to obtain the resolved-scale component $\tilde{\mathbf{u}}$ and a Langevin model to obtain the *sgs* velocity fluctuations $\mathbf{u}''$ [10, 12]. The velocity fluctuations are generated stochastically by assuming that the *sgs* contribution is isotropic and using a Gaussian distribution function at intervals coincident with the eddy-particle interaction time τ_i.

Instantaneous particle motions are tracked in the Lagrangian frame as they traverse a succession of *sgs* eddies. Particles are assumed to interact with these eddies for a time taken as the smaller of either the eddy lifetime or the characteristic transit time. The eddy lifetime τ_e is obtained using the scaling arguments embedded in the Smagorinsky model [24] to estimate the dissipation length scale ($L_e = \sqrt{C_I^3/C_R^2}\Delta$), and the model proposed by Yoshizawa [27, 28] to estimate the *sgs* kinetic energy ($k_{\text{sgs}} = C_I \Delta^2 \Pi_{\tilde{\mathbf{S}}}$). The term C_I (which appears in Yoshizawa's model) is calculated dynamically as a function of the trace of the Leonard stresses in a manner consistent with the evaluation of C_R. Applying this scaling yields the following expression for the eddy lifetime

$$\tau_e = \sqrt{\frac{3}{2}} \frac{C_I}{C_R} \Pi_{\tilde{\mathbf{S}}}^{-\frac{1}{2}}. \tag{16}$$

The characteristic transit time is obtained by equating the linearized form of Eq. (12) to the characteristic fluid speed in the eddy, L_e/τ_r, where the particle relaxation time τ_r is given by Eq. (13). This yields the expression

$$\tau_t = -\tau_r \ln \left(1 - \frac{L_e}{\tau_r |\mathbf{u} - \mathbf{u}_d|} \right). \tag{17}$$

The particle interaction time is obtained as a function of Eqs. (16) and (17) using the criteria

$$\tau_i = \begin{cases} \tau_e & L_e \geq \tau_r |\mathbf{u} - \mathbf{u}_d| \\ \\ \min(\tau_e, \tau_t) & L_e < \tau_r |\mathbf{u} - \mathbf{u}_d| \end{cases}. \tag{18}$$

When $L_e \geq \tau_r |\mathbf{u} - \mathbf{u}_d|$, Eq. (17) has no solution and it is assumed that the particle is entrained within the eddy. For the opposite situation it is assumed that the particle interacts with the eddy for a time taken as the smaller of the eddy lifetime or the characteristic transit time. Two-way coupling is achieved by simultaneously evaluating the source term given by Eq. (10) and the individual contributions imposed by each particle in term (i).

3. Results and Discussion

A schematic of the experimental apparatus and matching computational domain is shown in Fig. 1. The rig is cylindrical and consists of an injector section, main chamber, and plenum chamber. The coaxial injector houses a centered particle-laden primary jet surrounded by a swirling annular secondary jet. Flow is injected into the main chamber from the top. Upon entering the chamber the flow undergoes a sudden expansion followed by a series of complex fluid dynamic interactions. The flow then undergoes a second expansion at the exit of the main chamber into a plenum chamber.

The region of interest showing the eight axial stations where cross-sectional *PDA* measurements were made are shown in Fig. 2. Gas-phase and particle-phase mean and rms velocity components are given with simultaneous measurements of the particle size and mass flux distributions. Data were obtained with two different particle mass loadings in the primary jet, for three different particle size classes. The relevant flow conditions and particle properties are summarized in Table 1. Particles are injected into the primary jet in equilibrium with the gas phase velocity according to the distribution given by Fig. 3. This distribution produces a mean number diameter of $45\ \mu m$ and particle sizes over the range $20 \leq d_p \leq 80\ \mu m$, which is representative of typical fuel drop size distributions in gas turbine combustors. All of the walls inside the injector ducts are assumed to be adiabatic. The walls in the main chamber are assumed to be 300 *K*.

The geometry is characterized in dimensionless units using the radius R of the outer wall of the secondary jet as the reference length scale (i.e., $\delta_{\text{ref}} = R = 32\ mm$). The main chamber is approximately 30 dimensionless units long and extends a radial distance of approximately 3 dimensionless units. The injector section (not shown in Figs. 1 and 2) extends 8 units upstream from the main chamber face plate. The plenum chamber begins approximately 30 units downstream of the main chamber, ends at 50 units, and extends a radial distance of 9 units.

The primary jet has a radius of $r/R = 0.5$. Flow from the primary jet evolves to a fully-developed turbulent state prior to injection and enters the main chamber axially. The secondary jet extends over a radial interval of $0.59 \leq r/R \leq 1$, is fully-developed axially, and is injected into the main chamber with a swirling azimuthal velocity component. A reference velocity of $U_{\text{ref}} = 12.9\ m/s$ (based on the bulk flow rate in the primary jet) was used in all cases. The flow rate in the secondary annular jet was adjusted to give a maximum velocity of approximately $18\ m/s$. The maximum tangential velocity for both cases was approximately $13\ m/s$.

The grid used to perform the calculations includes the injector section, main chamber, plenum chamber and the upstream portion of the injector section not shown in the figures. This places the inlet plane of the primary and secondary jets at a location of 8 dimensionless units upstream of the entrance to the main chamber to provide the appropriate development lengths required to drive fully-developed turbulent flow in both ducts. The grid spacing in the primary and secondary jets were set by adhering to the requirements established to resolve the near-wall turbulence characteristics (i.e., "wall-resolved" LES). The azimuthal grid spacing was set using a uniform distribution of 64 cells. The grid density in the primary jet was set at $128 \times 64 \times 64$ in the axial, radial, and azimuthal directions, respectively. Similarly, the grid density in the swirling secondary jet was set at $128 \times 128 \times 64$. This distribution provides the level of fidelity required to resolve the turbulent Reynolds-stress tensor accurately. In each duct, the first cell from the wall was within a y^+ value of 1, the first 16 cells were within the interval $0 < y^+ < 30$, and the transverse grid spacing was set such that Δx^+ and Δz^+ where both less than 50.

The grid for the main chamber was constructed using the resolution requirements in the injector ducts as a baseline. The axial grid distribution was set by matching the spacing of adjacent cells in the injector section and stretching from the entrance of the main chamber the exit (where the flow is further expanded into the plenum). Stretching was accomplished by maintaining a relative factor of 1.02 between adjacent cells. The grid spacing in the radial direction was set by matching the radial distributions of the cells in the injector ducts at the inlet and filling in the remaining area by reflecting the stretching functions on adjacent sides of the ducts. The spacing on the plenum side of the main chamber was set to be uniform, with the inner distribution smoothly transitioned between these two end points. The resultant grid density in the main chamber is $128 \times 288 \times 64$.

The expansion induced by the plenum chamber has a significant influence on the upstream recirculation zones that form in main chamber. Thus, it is imperative that this section be included as part of the LES calculation to provide the correct unsteady pressure distribution across the exit plain of the main chamber. Significant errors can occur otherwise since a change in the overall structure of the recirculation zones induces a global shift in the location of the mean flow characteristics. Such a shift makes comparisons

between measured and modeled results meaningless. Here, we match the grid at the exit of the main chamber and stretch such that the entire plenum region is filled with a $32 \times 296 \times 64$ grid. The final grid of the entire domain is constructed with 4.4-million cells in total.

The Sommerfeld apparatus provides a particularly simple way to impose the upstream boundary conditions. The injector section is long enough to assume that fully-developed turbulent profiles exist at the inlets to the computational domain. With the added assumption that all wall surfaces are hydraulically smooth, we use the LES solver itself to drive fully-developed turbulence in the injector ducts. Fully-developed turbulent velocity profiles are generated inside the these ducts by recycling the unsteady velocity field from radial planes at an axial distance of 2 dimensionless units upstream of the main chamber face-plate. The stripped fields are corrected to maintain the mass flow rates specified in Table 1, then imposed at the injector inlet 8 units upstream with a non-reflecting pressure condition.

The secondary jet is corrected by modulating the azimuthal velocity in a manner that produces the correct experimentally measured swirl-number at the injector exit. This operation is performed using a simple control loop that converges on the azimuthal component of velocity required at the inlet to produce the preselected swirl numbers at the injector exit.

A representative LES solution corresponding to Case 2 in Table 1 is shown in Figure 4. This figure shows the instantaneous particle distribution in the region of interest superimposed on the corresponding turbulent velocity field in the y-x, z-x, and z-y planes corresponding to the axial locations of $x/R = 0.78,\ 1.6,\ 2.7$ and 3.5, respectively. The four radial cross-sections correspond to the axial stations where *PDA* measurements were made. This figure clearly highlights the asymmetric precessing nature of the flow. At any instant in time there are approximately 2.5-million particles being tracked in the region of interest. Tracking this number of particles is significant since it verifies the feasibility of employing large numbers of physical particles and eliminates the need to implement classical parcel approximations for cases such as this.

The mean flow characteristics are shown in Fig. 5. This figure shows the time-averaged gas-phase velocity field for both Case 1 (top) and Case 2 (bottom). Focusing first on Case 1, key features of the flow include the primary and secondary recirculation zones with cores centered at the $(x/R, r/R)$ coordinates of $(3.7, 2.0)$ and $(1.4, 2.4)$, respectively, the stagnation point in the core region centered at approximately $(3.3, 0.0)$ and the reattachment point centered at approximately $(2.5, 3.0)$. These numbers coincide with the measured results reported by Sommerfeld to within $5\ \%$. The highest negative velocities within the primary recirculation bubble are found at the coordinates $(3.7, 1.1)$.

Comparing the characteristics between Case 1 and 2 highlights the effect of particle loading on the mean flow characteristics. Particles, which initially have the same velocity as the air, are not able to follow the rapid expansion and deceleration of the gas jets upon injection into the main chamber. The larger particles have the highest velocities and tend to penetrate the central reverse flow region. The smaller particles tend to respond quickly to the recirculation of the gas flow and are more prone to entrainment in the secondary recirculation zone.

Direct comparisons between measured and modeled results for Case 2 are given in Figs. 6 through 10. Results in each of the figures coincide with the experimental measurement locations listed in Fig. 2. Figures 6 and 7 show comparisons of the mean and rms components of the axial, radial and azimuthal components of velocity. Symbols represent the measured data acquired by Sommerfeld *et al.*, the lines represent time-averaged LES results. Identical comparisons for the particle-phase are given in Figs. 8 and 9. Fig. 10 shows comparisons between the particle diameter and the momentum flux profiles. These data represent a small subset of the available results and provide a reasonable representation of the level of accuracy achieved in the simulations.

In all cases, the agreement between the measured and modeled results is excellent. We achieve the best agreement on the gas-phase mean values, which clearly falls within the experimental error bounds. Similar agreement is achieved with respect to the gas-phase rms values, with only slight degradation compared to the mean-values. Comparisons between the particle phase quantities are not quite as good, but exhibit similar

trends and are still well within the experimental uncertainties.

The agreement between the measured and modeled results shown in Figs. 6 through 10 is especially significant because there are no tuned constants used in any of the models. The only controlling parameters in the simulation are the grid spacing and implementation of boundary conditions. Thus, discrepancies can only be attributed to four possibilities: 1) bad numerics, 2) lack of appropriate grid resolution, 3) ill-posed implementation of boundary conditions, or 4) poor model performance. By implementing the approach described above, we are able to fairly confidently eliminate the all but the last prior to performing the calculation. We can further conclude, based on the agreement between the measured and model results, that the current modeling approach performs relatively well for multiphase flow under lightly loaded conditions and approaches a predictive capability for the conditions cited.

With this confidence in place, we are able to extract additional information from the calculations that cannot be measured experimentally to gain further insights relevant to modeling sprays. As one example, there are two relevant sets of information of leading significance. The first is the local instantaneous particle Reynolds number exhibited by particles in the region of high-shear between the primary and secondary recirculation zones. The second is the corresponding Kolmogorov length and time scale distributions in the same region. Figures 11 and 12 provide this information.

Figure 11 shows profiles of the mean and rms particle Reynolds number extracted from the LES. The solid curves represent the bulk average over all particle diameters, d_p, the dashed curves represent $d_p = 30 \pm 5\ \mu m$, dash-dot represent $d_p = 45 \pm 5\ \mu m$, and dash-dot-dot represent $d_p = 60 \pm 5\ \mu m$. Examining these profiles in the high-shear region at $x/R = 0.78$ indicates that the larger particles exhibit a higher mean Reynolds number with peak values of approximately $Re_p = 70 \pm 20$, while the smaller particles exhibit peak values of $Re_p = 20 \pm 10$.

Estimations of the corresponding Kolmogorov length and time scales in the region of interest are shown in Fig. 12. These data have been non-dimensionalized by the reference length scale $\delta_{\text{ref}} = R = 32\ mm$ and characteristic time scale $\tau_f = \delta_{\text{ref}}/U_{\text{ref}} = 2.48\ ms$, where $U_{\text{ref}} = 12.9\ m/s$ (as defined above). In the high-shear region at $x/R = 0.78$, the Kolmogorov length and time scales approach values as small as $0.01\ mm$ and $0.1\ ms$. These quantities represent the smallest limiting extreme for this particular case.

4. Conclusions

In the sections above we have established a groundwork for simulating complex wall bounded turbulent flows, non-reacting particle-laden flow, and recirculating swirling flow with characteristics relevant to gas turbine (and similar) combustors. We have highlighted a systematic approach for validating the accuracy of LES in a progressive manner with well-defined and carefully implemented boundary conditions.

The validated case study provides a mechanism to establish baseline numerical capabilities, to gain a clearer understanding of the effectiveness and feasibility of current models, and to gain a more quantitative understanding of relevant modeling issues by analyzing the characteristic parameters and scales of importance. Future work will focus on continued systematic assessments and validation of physical models in both multiphase and reacting multicomponent systems.

Acknowledgments

The U. S. Department of Energy, Office of Basic Energy Sciences, Division of Chemical Sciences, Geosciences, and Biosciences supported this work. Sandia National Laboratories is a multiprogram laboratory operated by Sandia Corporation, a Lockheed Martin Company, for the United States Department of Energy under contract DE-AC04-94-AL85000.

References

[1] M. Sommerfeld, H. H. Qiu, *International Journal of Heat and Fluid Flow* 12 (1) (1991) 20–28.
[2] M. Sommerfeld, A. Ando, D. Wennerberg, *Journal of Fluids Engineering* 114 (1992) 648–656.
[3] M. Sommerfeld, H. H. Qiu, *International Journal of Multiphase Flow* 19 (6) (1993) 1093–1127.
[4] J. K. Eaton, J. R. Fessler, *International Journal of Multiphase Flow* 20 (1) (1994) 169–209.
[5] M. R. Maxey, B. K. Patel, *International Journal of Multiphase Flow* 27 (9) (2001) 1603–1626.
[6] A. Ferrante, S. E. Elghobashi, *Physics of Fluids* 15 (2) (2003) 315–329.
[7] J. C. Oefelein, V. Yang, *Simulation of High-Pressure Spray Field Dynamics, Recent Advances in Spray Combustion, Spray Combustion Measurements and Model Simulation*, Vol. 171 of *Progress in Astronautics and Aeronautics*, American Institute of Aeronautics and Astronautics, New York, New York, 1995, Ch. 11, pp. 263–304.
[8] J. C. Oefelein, *Proceedings of the 12th Annual Conference on Liquid Atomization and Spray Systems* (1999) 143–147Institute of Liquid Atomization and Spray Systems (ILASS), Indianapolis, Indiana.
[9] S. V. Apte, K. Mahesh, P. Moin, J. C. Oefelein, *International Journal of Multiphase Flow* 29 (8) (2003) 1311–1331.
[10] J. C. Oefelein, *Simulation and Analysis of Turbulent Multiphase Combustion Processes at High Pressures*, Ph.D. thesis, The Pennsylvania State University, University Park, Pennsylvania (May 1997).
[11] J. D. Kulick, J. R. Fessler, J. K. Eaton, *Journal of Fluid Mechanics* 277 (1994) 109–134.
[12] J. C. Segura, J. K. Eaton, J. C. Oefelein, *Predictive Capabilities of Particle-Laden Large Eddy Simulation*, Tech. Rep. TSD-156, Department of Mechanical Engineering, Stanford University, Stanford, California (2004).
[13] A. Paris, J. K. Eaton, *Turbulence Attenuation in Particle-Laden Channel Flow*, Tech. Rep. TSD-137, Department of Mechanical Engineering, Stanford University, Stanford, California (2001).
[14] M. Benson, J. K. Eaton, *The Effects of Wall Roughness on the Particle Velocity Field in a Fully-Developed Channel Flow*, Tech. Rep. TSD-150, Department of Mechanical Engineering, Stanford University, Stanford, California (2003).
[15] J. C. Oefelein, *General Numerical Framework for Reacting Multiphase Flow with Complex Thermochemistry, Thermodynamics and Transport*, copyright 1992-2005 by J. C. Oefelein, All Rights Reserved (2005).
[16] J. C. Oefelein, *General Package for Evaluation of Multicomponent Real-Gas and Liquid Mixture States at All Pressures*, copyright 1992-2005 by J. C. Oefelein, All Rights Reserved (2005).
[17] G. Erlebacher, M. Y. Hussaini, C. G. Speziale, T. A. Zang, *Journal of Fluid Mechanics* 238 (1992) 155–185.
[18] C. G. Speziale, *Journal of Fluid Mechanics* 156 (1985) 55–62.
[19] M. Germano, U. Piomelli, P. Moin, W. H. Cabot, *Physics of Fluids* 3 (7) (1991) 1760–1765.
[20] P. Moin, K. Squires, W. Cabot, S. Lee, *Physics of Fluids* 3 (11) (1991) 2746–2757.
[21] D. K. Lilly, *Physics of Fluids* 3 (11) (1992) 633–635.
[22] Y. Zang, R. L. Street, J. R. Koseff, *Physics of Fluids* 5 (12) (1993) 3186–3195.
[23] B. Vreman, B. Geurts, H. Kuerten, *Physics of Fluids* 6 (12) (1994) 4057–4059.
[24] J. Smagorinsky, *Monthly Weather Review* 91 (1963) 99–164.
[25] C. T. Crowe, M. P. Sharma, D. E. Stock, *Journal of Fluids Engineering* 99 (1977) 325–332.
[26] R. Clift, J. R. Grace, M. E. Weber, *Bubbles, Drops, and Particles*, Academic Press Incorporated, New York, New York, 1978.
[27] A. Yoshizawa, *Physics of Fluids* 27 (6) (1984) 1377–1387.
[28] A. Yoshizawa, *Physics of Fluids* 29 (7) (1986) 2152–2164.

List of Tables

List of Figures

Table 1: Flow conditions and particle properties used in the Sommerfeld experiments.

	Case 1	**Case 2**
Gas Phase (Air):		
Flow rate in primary jet, g/s	9.9	6.0
Flow rate in secondary jet, g/s	38.3	44.6
Inlet Reynolds number[a]	26200	27250
Swirl number	0.47	0.49
Temperature, K	300	
Particle Phase:		
Loading ratio in primary jet	0.034	0.17[b]
Flow rate, g/s	0.34	1.0
Mean diameter, μm	45.5	
Density ratio, ρ_p/ρ_f	2152	

[a] Based on total volume flow rate.

[b] $5 \times$ Case 1.

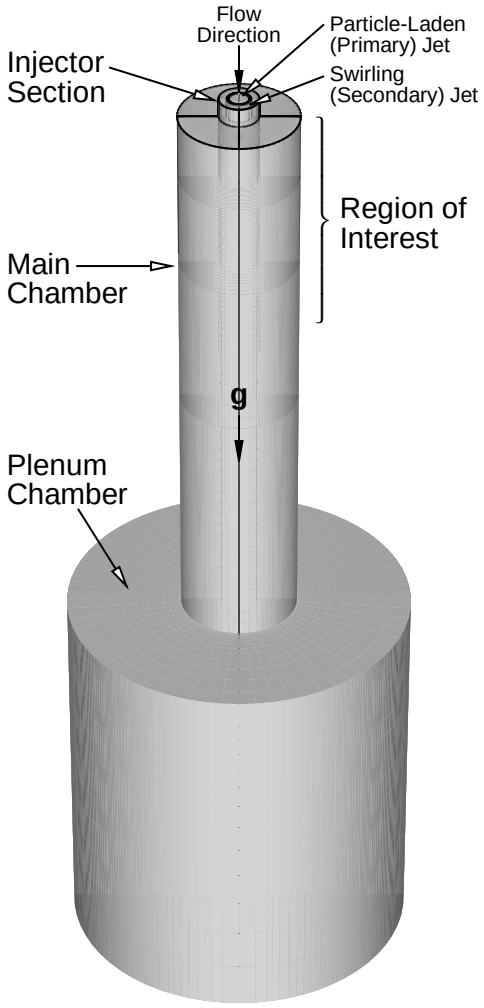

Fig. 1: Schematic of the experimental apparatus employed by Sommerfeld *et al*. [1–3].

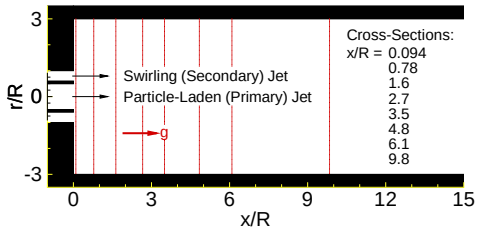

Fig. 2: Region of interest showing the location where cross-sectional *PDA* measurements were made.

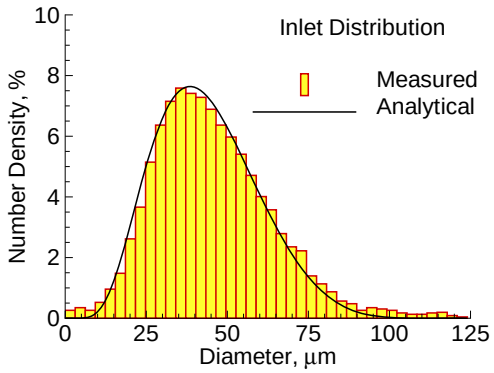

Fig. 3: Particle size distribution in the axial (primary) jet.

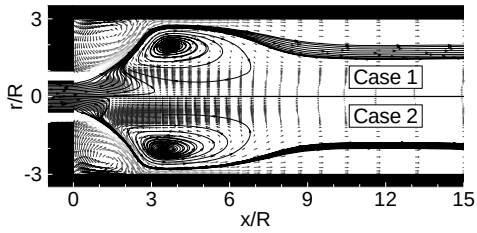

Fig. 5: Time-averaged flow characteristics associated with Case 1 (top) and Case 2 (bottom).

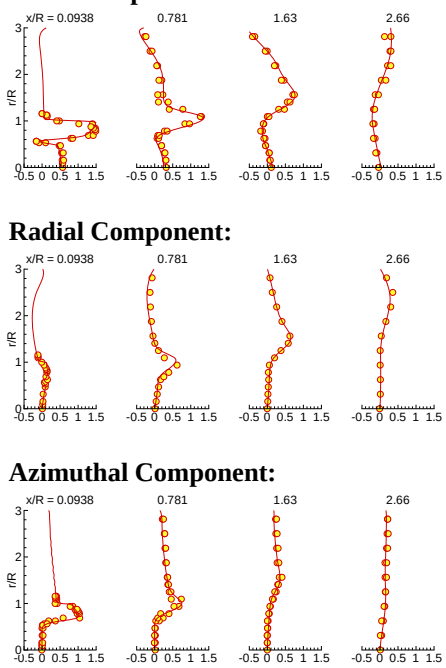

Fig. 6: Time-averaged profiles of the dimensionless gas-phase velocity field (Case 2). Symbols represent measured data from Sommerfeld *et al*. [1–3], lines represent LES results.

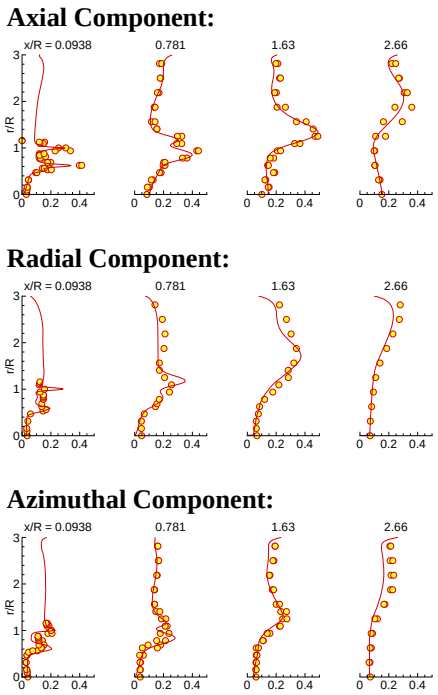

Fig. 7: RMS profiles of the dimensionless gas-phase velocity field (Case 2). Symbols represent measured data from Sommerfeld *et al*. [1–3], lines represent LES results.

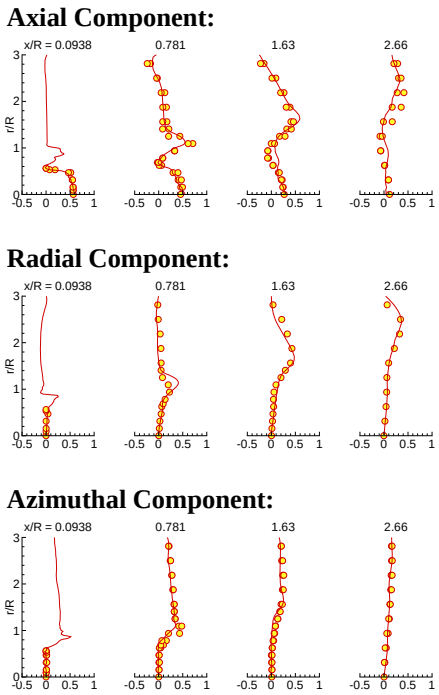

Fig. 8: Time-averaged profiles of the dimensionless particle-phase velocity field (Case 2). Symbols represent measured data from Sommerfeld *et al*. [1–3], lines represent LES results.

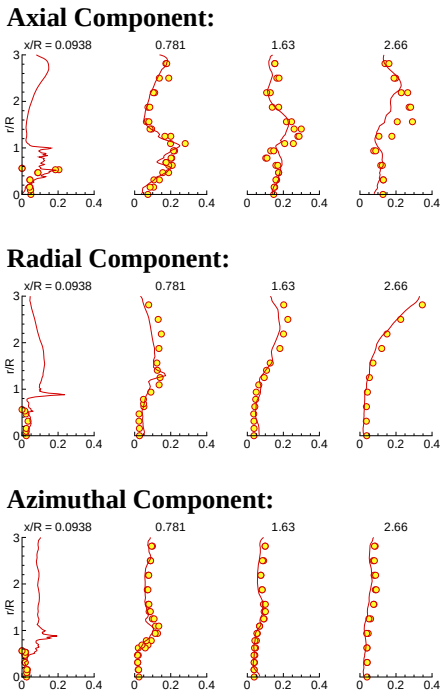

Fig. 9: RMS profiles of the dimensionless particle-phase velocity field (Case 2). Symbols represent measured data from Sommerfeld *et al*. [1–3], lines represent LES results.

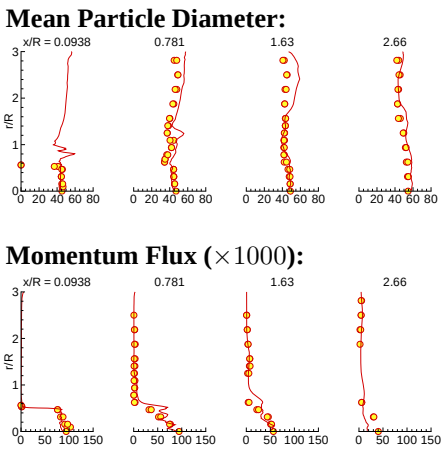

Fig. 10: Dimensionless particle diameter and momentum flux profiles (Case 2). Symbols represent measured data from Sommerfeld *et al*. [1–3], lines represent LES results.

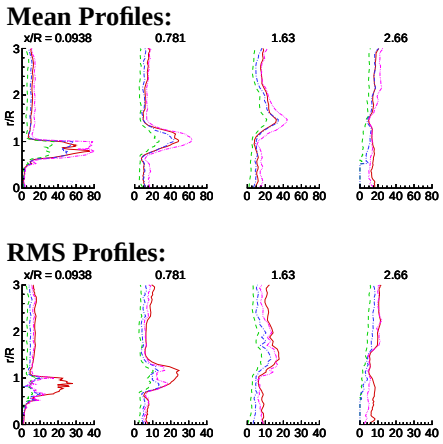

Fig. 11: Mean and RMS profiles of particle Reynolds number extracted from the LES (Case 2). The solid curve represents the bulk average over all particle diameters, d_p, the dashed curve represents $d_p = 30 \pm 5\ \mu m$, dash-dot represents $d_p = 45 \pm 5\ \mu m$, and dash-dot-dot represents $d_p = 60 \pm 5\ \mu m$.

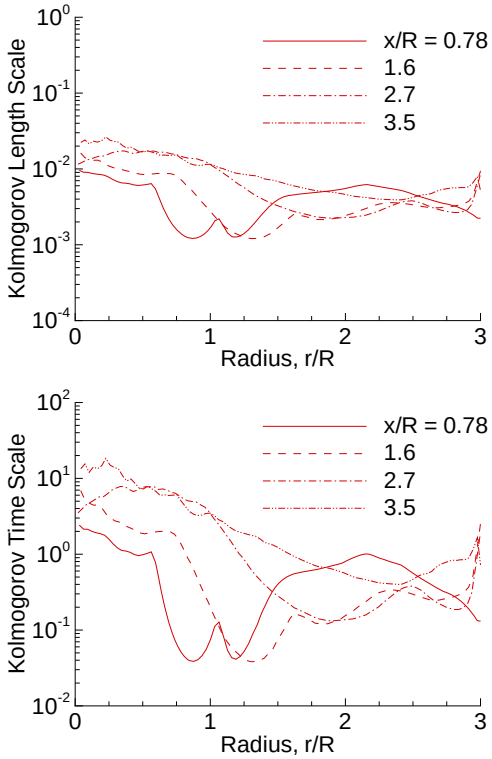

Fig. 12: Dimensionless Kolmogorov length and time scales in vicinity of high-shear region.